

Enhanced magnetoelastic stress in disordered iron-gallium alloy thin films revealed by direct measurement.

Adrián Begué^{a,1}, Maria Grazia Proietti^a, José Ignacio Arnaudas^a, Miguel Ciria^{a,2}

^aInstituto de Nanociencia y Materiales de Aragón (INMA), CSIC-Universidad de Zaragoza, Spain.

Abstract

The large magnetostriction in FeGa alloys is relevant for manifold applications, but for thin films, it can play a prominent role in controlling the strength of the magnetic anisotropy. Bulk samples show values depending on the extensive preparation procedure compendium, which is limited in its temperature range for high-quality thin-film synthesis. Here, we present a study of the magnetoelastic coupling coefficients B_1 and B_2 in epitaxial FeGa thin films below 50 nm deposited on the MgO(001) surface at 150 °C by the cantilever method. Series of films with 22, 28, and 33 at. % Ga do not show thickness-dependent variations for B_1 and B_2 , but $-B_1$ for the 22 at. % Ga composition is 10 MPa, roughly 2 times the bulk value and smaller than the bulk-like value of $-B_1=12.1$ MPa obtained for a film with 17 at. % Ga. This enhancement is correlated with the A2 crystal structure for the film rather than the coexistence with $\text{D}0_3$ or other ordered nanometric precipitates proposed for bulk samples. Synchrotron diffraction excludes the formation of long-range $\text{L}6_0$, or $\text{D}0_3$ precipitates in samples with (001)A2 peaks at concentrations around 25 at. % Ga, which implies partial chemical disorder. The analysis of extended x-ray absorption fine structure measurements points to a $\text{D}0_3$ local order with a residual number of Ga-Ga pairs. Considering that the substrate quenches the movable strain in the A2 phase described in dual-phase structures, our results point to the important role of the electronic structure of the iron atoms modified by the presence of Ga in the alloy. This effect enlarges B_1 in films with the A2 phase, stabilized using epitaxial growth.

Keywords: Fe-Ga alloys, magnetoelasticity, thin films, X-ray diffraction, EXAFS

1. Introduction

The $\text{Fe}_{100-x}\text{Ga}_x$ ($x < 35$) alloy family displays compelling properties to be used in elements looking for energy-efficient applications. The compound with $x \approx 18$ was first known for large values for the tetragonal magnetostrictive mode λ_{100} [1, 2], a property that coincides with small values for the lowest order magnetic anisotropy constant K_1 [3]. Its use in magnetolectric heterostructured materials for voltage control of the magnetization based on strain-induced coupling between ferroelectric and magnetostrictive components has demonstrated large converse coupling, with coefficient values well above 10^{-5} ms^{-1} [4, 5], a feature fundamental to reduce the energy consumption in processing information [6] and neuromorphic computing [7]. On the other hand, the ordered $\text{D}0_3$ phase ($x \sim 25$) presents a stark giant anomalous Nernst effect at room temperature [8] suitable for recollecting energy using thermal variations due to the probable presence of a topological nodal-web structure [9].

The enhancement of λ_{100} in FeGa alloys with respect to the pure iron value has been explained using several frameworks. The idea of local order occurring by the generation of nanometric particles of a second phase [10–15] or the electronic structure modification on the Fe atoms [16–21] makes the FeGa

alloys an archetype dual-phase systems. On one side, the presence of inclusions with a tetragonal symmetry, $\text{D}0_{22}$ and $\text{L}6_0$ (or $\text{mD}0_3$, see figure 1a) in the cubic A2 matrix activates a strain in the matrix that enlarges the deformation in the single domain configuration [12]. The role of the tetragonal inclusions as the seed of the enhanced magnetostriction with the rotation of their anisotropy axis by the magnetic field [22] or induced strain around the particles in the A2 matrix, which rotates and follows the magnetic field [12, 15], are also under discussion. However, although the more significant increment of λ_{100} with $x < 20$ appears for samples obtained with a quenching from a high-temperature mix, λ_{100} also takes values higher than that for iron for slow cooling metallurgic processes [23]. In any case, high photon flux experiments suggest that the volume fraction of $\text{mD}0_3$ is below 0.2% due to the lack of pristine observation of the distinctive reflections [24]. Evaluating B_1 by the indirect method of measuring the magnetic anisotropy suggests an enhancement associated with the A2 phase stabilized by epitaxial growing for $x > 20$ [5]. On the other side, extensive *ab initio* studies [16–21] look into the modification of the Fe electronic state and its influence in the magnetoelastic (ME) coupling coefficient B_1 and stiffness elastic coefficients c_{11} , c_{12} , $(3/2)\lambda_{100} = -B_1/(c_{11} - c_{12})$ as a function of the Ga content, and the presence of others 3d and 4f ions in the A2 phase, as well as the calculation of those coefficients for the B2 and $\text{D}0_3$ crystal structures.

The complexity in finding a satisfactory explanation for the

¹Current address: Laboratoire Albert Fert, CNRS, Thales, Université Paris-Saclay, 91767 Palaiseau, France

²Corresponding author: miguel.ciria@csic.es

enhancement of λ_{100} in Fe alloys reveals a rich behavior in samples prepared under different procedures that can not be replicated for thin films. Interestingly, in bulk samples, the density of those nano inclusions involves annealing at high temperatures (1000 °C), quenching and aging at intermediate temperatures, and a second quenching [25]. These procedures are not accessible for thin film preparation aiming for flat topography and sharp interfaces since inter-diffusion with the substrate or buffer layers or the formation of rough layers with dome-like topography is activated by substrate temperature [26]. In any case, in the nanometric range, FeGa crystalline films with low magnetic anisotropy show an ME stress large enough to activate uniaxial magnetic anisotropies [4, 5] by piezostains and/or ferroelastic strain, with large converse magnetoelectric coupling coefficients. The magneto-crystalline barrier for moving M in the (001) plane between easy and hard direction is ($K_1/4$), which is below 10 kJm^{-3} for $x > 18$ [3] and 1 kJm^{-3} for $x > 25$ [27]. It can be overcome if uniaxial strain as low as 0.001 is applied, considering that $-B_1$ can take values around 10 MPa, which is a value not unusual for thin films [5, 28] and about 4 times the Fe bulk value [29].

The effect of the epitaxial strain induced on the film introduces an environment different from that proposed for bulk samples. The induced strain by nano inclusions, if they nucleate, may be concealed in very thin films: the internal strain is generated by the misfit with the substrate, and inhomogeneities are tied either to the relaxation of the strain through misfit dislocations of elastic deformation. The effect of the substrate can be released as the thickness of the film increases, as is shown by the increment of the temperature at which the lattice parameter is frozen by the substrate on Eu films [30]. Therefore, the substrate restricts the rotation of distortions in the crystalline A2 matrix or the embedded nanoparticles for very thin films. The origin of the observed stress, which occurs when a magnetic field is applied and moves the magnetization away for the easy direction, highlights the significant role of an electron-like mechanism based on spin-coupling, primarily due to the introduction of gallium. That scenario is also different from the one observed in polycrystalline thin films: the effective ME coefficient $|B_{eff}|$ yields increasing [31] or decreasing [32–34] values with increasing film thickness, that can be associated to modification of the crystal orientation of the grains or Néel surface contributions. Also, the strain-stress states of the grains in polycrystalline films induced by the substrate can be relevant in the observed value of B_{eff} [35].

Before dealing with the enhancement of λ_{100} in FeGa alloys, it is worth mentioning the complexity of the magnetostriction phenomena of the single Fe element. It is known that B_1 shows a very unusual temperature dependence without decreasing B_1 as T rises from 0 K to room temperature. That departure from Akulov’s law [29], which introduces the thermal disorder in the orientation of the magnetic moment, forced to consider shifts of the orbital levels as a function of the temperature to explain that behavior [19, 36]. Also, a strain-sensitivity of the ME coupling coefficients B_1 and B_2 is demonstrated by the observation of decrements of the $|B_1|$ and B_2 bulk values for Fe films with thickness even above 100 nm grown on MgO(001) [37, 38].

Motivated by the strain-induced results observed in FeGa thin films, the phenomenology associated with the local order chemical as well and the lack of measurements of the fundamental magnetoelastic coefficients for films below 50 nm, we report direct measurements of B_1 and B_2 in epitaxial thin films grown on MgO(001) substrates, complemented with extended x-ray absorption fine structure measurements for the same set of samples. Therefore, measuring the B ’s is of interest since the softening of the $c_{11} - c_{12}$ coefficient is the one reason for the observation of the second peak in the λ_{100} vs x curve and also contribute partially to enhance λ_{100} around $x = 19$ [2].

2. Materials and methods

2.1. Thin film preparation

The procedure to obtain $\text{Fe}_{100-x}\text{Ga}_x$ crystalline films onto MgO(001) crystals has been described elsewhere [39]. The film composition was set by co-evaporation of Ga and Fe using effusion cells and ebeam gun. The films were grown at a substrate temperature of 150 °C and have thicknesses below 60 nm. The FeGa[100] in-plane direction is aligned with the MgO [110] axis. Two rectangular MgO(001) plates with edges along [110] and [100] were used to obtain films suitable to measure B_1 and B_2 , respectively, on films grown in the same batch. The structure of the layers is monitored *in situ* using Reflection High Electron Energy Diffraction (RHEED), with electron beam energy equal to 15 keV, see Fig. 1b. Continuous substrate rotation was enabled to improve the homogeneity of every layer.

Three sets of films with $x \approx 22, 28,$ and 33 and film thickness range between 10 nm and 50 nm were studied, as well as several films with thickness around 50 nm and varying Ga concentration. Table 1 shows the relation of films studied in this work and some relevant parameters such as thickness and estimated composition obtained by energy-dispersive X-ray spectroscopy (EDX) and Wavelength Dispersive Spectroscopy (WDS) in an electron probe micro-analyzer (EPMA) instrument.

2.2. Characterization techniques

XRD diffraction was performed in the Bragg-Brentano configuration with a RIGAKU Ru2500 diffractometer (copper anode 40 kV/80 mA, with $\lambda = 1.54 \text{ \AA}$) and synchrotron radiation (BM25 Spain Beamline at ESRF, with $\lambda = 0.62 \text{ \AA}$). X-ray reflectometry was used to obtain the film thickness by fitting the intensity oscillations using a Bruker D8 diffractometer, Fig. 1c. X-ray Absorption Fine Structure (XAFS) spectroscopy is a short-range-order, chemically selective technique complementary to diffraction. It can provide information on the atomic local environment of the different atoms comprising the samples (see ref [40] for an overview). The XAFS spectra $\mu(E)$ were recorded with the beam polarization nearly parallel (ϵ_{\parallel} , incidence angle $\cong 5^\circ$) and almost perpendicular (ϵ_{\perp} , incidence angle $\cong 85^\circ$) to the sample surface. We measured the extended region above the absorption edge of the XAFS spectrum (EXAFS) and the Near-Edge region (XANES) at the Fe and Ga K-edges at beamline B18 of the Diamond UK’s National Light Source. The raw

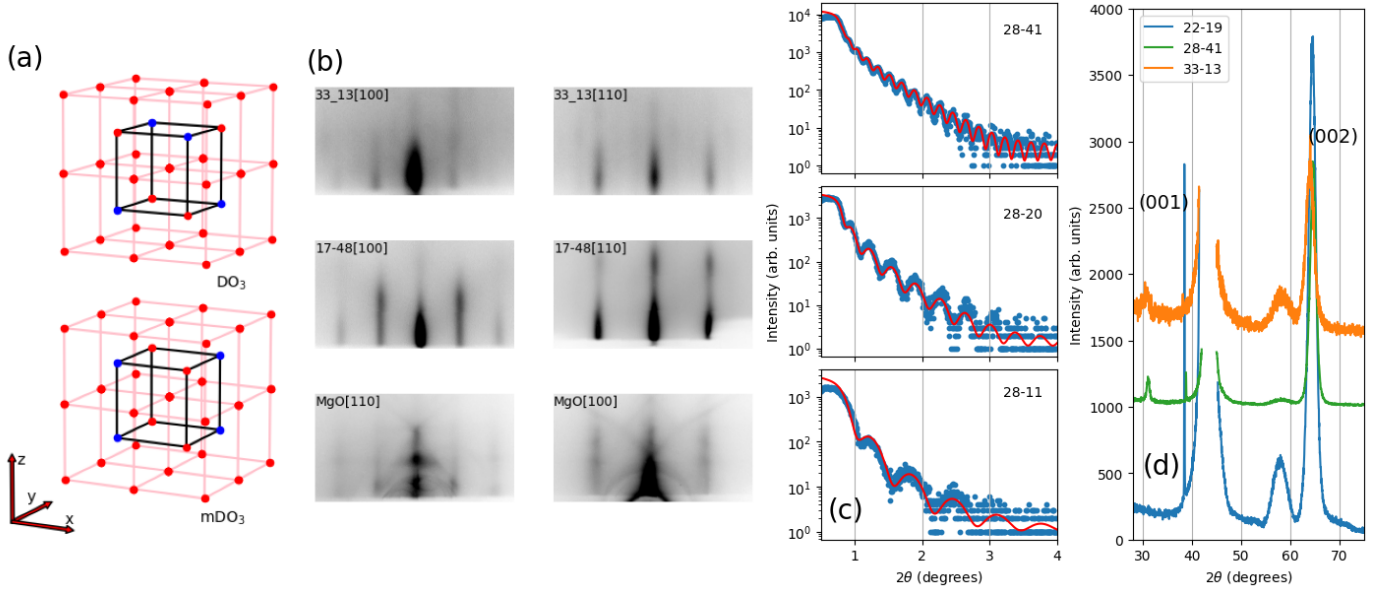


Figure 1: (a) Sketch of the mDO_3 and DO_3 structures, (b) RHEED images of the FeGa alloy and the MgO substrate before the film evaporation. (c) XRR data (dots) and fit (red line) performed to obtain the film thickness (d) Bragg-Brentano scans for films with and without the presence of the superlattice peak at $2\theta \approx 30.6^\circ$.

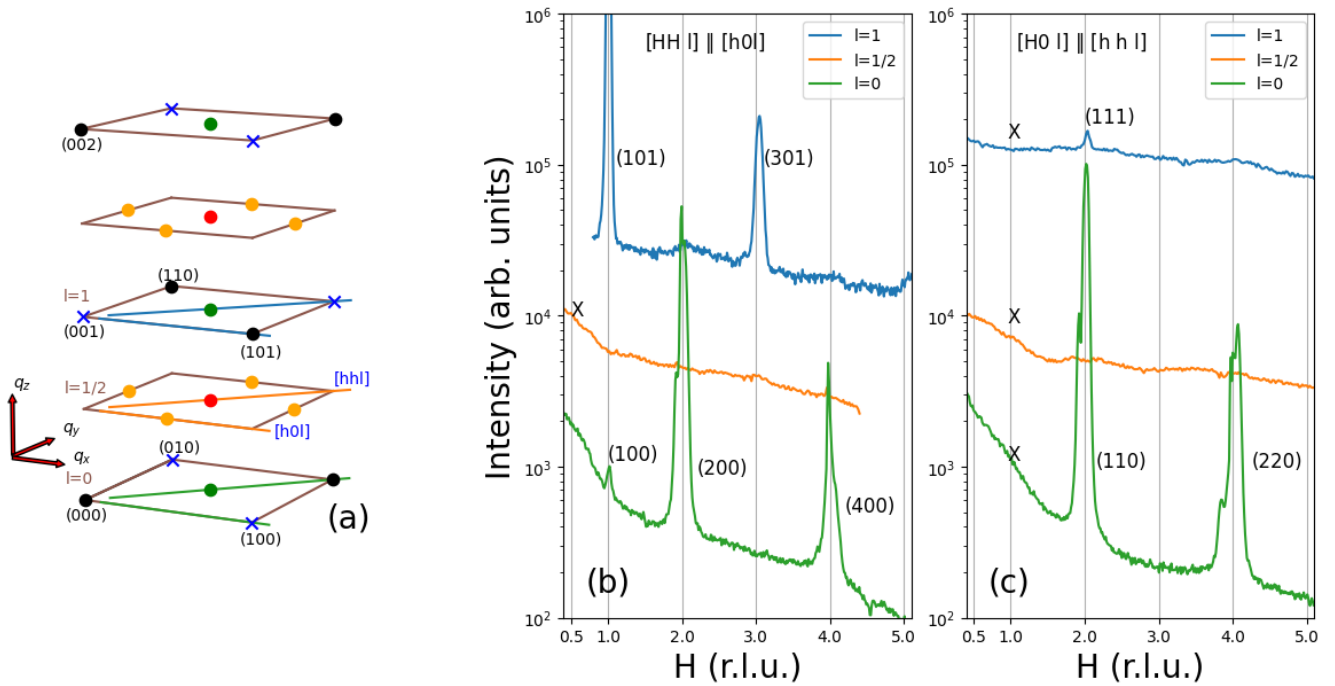


Figure 2: (a) Sketch of the reciprocal space for the A_2 (black points) B_2 (black points and crosses), DO_3 (black points, crosses, and red points) and mDO_3 (black points, crosses, and green points) with variants with Ga-pairs along the z Cartesian axes (Figure 1a). For in-plane Ga-pairs, yellow points appear instead of green ones. The reference axes correspond to the FeGa structure. Reciprocal space linear scans along (b) $[HH\ l] \parallel [h0l]$ with $l = 0, 1/2$ and 1 ; and (c) along $[H0\ l] \parallel [h\ h\ l]$ with $l = 0, 1/2$ and 1 . The parameter H is the Miller index of the MgO cubic lattice and the reciprocal lattice has units of $2\pi/a_{MgO}$. The labels close to the peaks indicate Miller indexes of observed FeGa reflections. Crosses are located at positions where extra reflections identifying the DO_3 or mDO_3 structures should have been observed.

Sample	thickness (nm)	x (% Ga)	$-B_1$ (MPa)	B_2 (MPa)
Fe	73	0	2.1	5.5
17-48	48	17.2	12.1	6
22-10	10.6	22	9.5	1.5
22-19	19.0	22	10.3	1.6
22-33	32.6	22	10.3	1.3
28-11	10.8	28	6.1	-5.3
28-20	20.0	28	5.9	-4.8
28-31	31.8	28	7.4	-4.8
28-41	41.1	28	6.5	-5.3
33-13	13.0	33	5.9	-3.9
33-25	25.0	33	6.2	-3.9
33-36	35.7	33	7.4	-3.5
26-52	52	26	-	-4.4

Table 1: Set of films measured in this work. The code identifies samples by composition x and thickness. The values of B_1 and B_2 are also indicated.

polarized XANES spectra with parallel and perpendicular polarization were subtracted from each other to obtain the Linear Dichroism XANES signal (LDXANES) [41].

Magnetic hysteresis loops were obtained by using a magneto-optical Kerr effect (MOKE) magnetometer (nanoMoke3) with the field H in the film plane, see Figure 5. Also, from the hysteresis loops the energies requested to saturate the film are estimated by evaluating the area $A(\phi)$ of the anhysteretic curve and the bulk magnetization value M_s . Thus, the lowest order magnetic anisotropy constant K_1 is calculated as $A([110]) - A([100]) = K_1/4$. All the films were studied using the cantilever method with a magnetic field rotation of about $\mu_0 H = 100$ mT. The rotation of the field is required to extract the magnetization \mathbf{M} from the easy direction since if $\mu_0 H$ is applied along the easy axis, the inversion of \mathbf{M} takes place suddenly at the coercive field but without strain change, since a 180° domain wall movement can take place to switch \mathbf{M} and $\lambda \propto M^2$. See the appendix for details relating the magnetoelastic stresses with the cantilever capacitive detection method.

3. Results and discussion

3.1. X-ray diffraction characterization

XRD scans in the Bragg-Brentano configuration show the FeGa (002) and the Mo (002) reflections around $2\theta \approx 64^\circ$ and 58° , respectively, and above $x = 22$ the (001) one at $2\theta \approx 30.6^\circ$, see figure 1d. The latter weak reflection indicates ordering between the Fe and Ga species, and it is common to B2, D0₃, and mD0₃ structures. Those weak peaks are labeled as superlattice (SL) reflections to distinguish them from the strong reflections originating from the A2 structure. The corresponding out-of-plane lattice parameters, obtained from the (002) reflection, are between 2.88 Å and 2.91 Å, which are values smaller than those observed for bulk samples with the same composition [42]. Thus, see Figure 1d, samples 22-19 ($2\theta = 64.58^\circ$), 28-41 ($2\theta = 64.68^\circ$) and 33-47 ($2\theta = 63.94^\circ$) yield 2.88 Å, 2.88 Å and 2.91 Å respectively. The bulk value for $x=23$ is about 2.91 Å. The (001) peak is observed at $2\theta = 31.116^\circ$ for

the 28-41 film and $2\theta = 30.58^\circ$ for the 33-47 one. The films studied here do not show the presence of phases with the fcc-like arrangement of the atoms observed by the presence of the (002) reflections around $2\theta \approx 49^\circ$ ($a \approx 3.69$ Å) [39, 42].

X-ray diffraction employing synchrotron radiation was used to look for SL reflections characteristic of D0₃ and mD0₃ structures, see Figure 2, in the 26-52 film, with the (001) reflection observed in the Bragg-Brentano configuration. Here, we use the notation h, k, and l for the Miller indices for the A2 reciprocal space lattice, space group $Im\bar{3}m$, $Z = 2$ and unit vector $2\pi/a$, with a the lattice parameter to be obtained but around 2.9 Å. The B2 structure, space group $Pm\bar{3}m$ implies an order between Fe and Ga in the cell and many Ga-Ga pairs. For the D0₃ and mD0₃, the cell unit is doubled in real space, see Fig.1a, and ordering appears with fractional values of h, k, and l [43]. Using the D0₃ cell avoids the fractional notation and is straightforwardly done by multiplying by two the Miller indices. Figure 2.a shows a sketch of the reciprocal space with the reflections due to the A2 phase ($h+k+l = \text{even}$, black points) and SL reflections. For B2 crosses are added at $h+k+l = \text{odd}$; for the D0₃ phase distinguished reflections are added at $[1/2](h\ k\ l)$, the red points, while for mD0₃ those specific SL peaks correspond to the green points at $(h+0.5\ k+0.5\ l)$ for pairs along the [001], and $(h+0.5\ k\ l+0.5)$ or $(h\ k+0.5\ l+0.5)$ for in-plane [010] and [100] Ga pairs, see orange points. The lines indicate scans performed with synchrotron radiation to ascertain the presence of the D0₃ or mD0₃ phases and presented in Fig2 a and b. Those scans use the MgO crystal to set the reference frame (with H, K, and L Miller indices and $2\pi/a_{MgO}$ modulus of the unit cubic vector). The epitaxy between the MgO [110] parallel to the FeGa [100] of the bcc structure is observed at the scans with $L \approx 0$, where peak overlapping is manifested, see Fig.2 b and c. Therefore, for scans along [HH.], $h \approx H$, while for [H0.] $h=k \approx 2H$. The more intense peaks correspond to the Bragg condition for the bcc lattice ($h+k+l = \text{even}$). Thus, [HH.] is parallel to [h0.], and the value of L for the FeGa reflection ($l=1,2$, etc.) is determined by maximizing the intensity for the FeGa (002) reflection. For $l=1$, blue lines, the A2 (101), (301), and (501) reflections, and the SL peak (111) are visible.

The scans [hh 1] (blue line) and [h0 1/2] (orange line) did not show $(1/2\ 1/2\ 1)$ and $(1/2\ 0\ 1/2)$ contributions from mD0₃ with [001] and in-plane Ga-pairs, respectively. On the other hand, the scan [hh 1/2] (orange line) discards the D0₃ phase by the absence of the $(1/2\ 1/2\ 1/2)$ peak. The scans at grazing incidence ($l \approx 0$, green lines) only show the (100) peaks but not $(1/2\ 1/2\ 0)$ corresponding to the mD0₃ with [001]Ga-pairs. The lack of SL peaks in epitaxial alloy films has also been observed in Heusler compounds. It suggests the presence of chemical disorder in the structure [44]. Therefore, (001) planes of Fe atoms sandwiched between a single atomic layer of a disordered mixture of Fe and Ga atoms generate a B2-like structure that excludes the formation of long-range D0₃ or mD0₃ structures (see Fig. 1a). Interestingly, the growth at 150°C shows the well-known trend of Ga to avoid other Ga as the first neighbor. However, at that temperature, the formation of long-range order in the FeGa layer is inhibited. These scans allow determining the out-of-plane and in-plane lattice parameters result-

ing in a value of 2.88 Å and 2.93 Å respectively, and demonstrating a tetragonal deformation of the cubic cell enlarging the in-plane distances due to the epitaxy with the in-plane distance of the MgO substrate ($a_{MgO} = 4.212$ Å, $\sqrt{2}a_{FeGa} \approx 4.1$ Å)

3.2. EXAFS Results

The experimental spectra were fitted by theoretical EXAFS signals calculated by *ab initio* theoretical phase and amplitudes generated for a cluster of 78 atoms with a radius of 6.1 Å⁻¹, by the TKAtoms code [45]. The central absorber was a Ga or Fe atom with only one kind of Ga (Fe) scatterer. The alloying FeGa effect was obtained by combining the pure Ga-Fe(Ga) and Fe-Fe(Ga) systems at the Ga and Fe K-edge, respectively. The 8.01 Feff code generated the theoretical phase-shifts and amplitudes [46] taking into account beam polarization. The DEMETER package was used for extraction and best-fit procedure of the EXAFS spectra [47].

The raw EXAFS spectra were Fourier Transformed (FT) in the range $2 < k < 11$ Å⁻¹. Figure 3a shows raw background subtracted EXAFS spectra at the Ga K-edge, and Fig. 3b, the correspondent FT signals, for the two beam polarization directions. The first peak of the FT spectra is due to the first and second coordination shells. The contributions of next neighbor (NN) and next-nearest-neighbor (NNN) atoms are merged into a single FT peak due to the proximity of the interatomic distances values (2.48 Å and 2.87 Å respectively in pure bcc Fe) and the limited transformation range. The best-fit analysis was performed simultaneously for the two polarizations in q-space, by Fourier Filtering of the first peak contribution in the range $1 < R < 3$ Å. The best-fit parameters were: the origin of the photoelectron energy E_0 , the Ga population in NN and NNN environments, x_I and x_{II} , the interatomic distances of first, d_I , and in-plane second $d_{I||}$ coordination shell, and the Debye-Waller factors. The S_0^2 amplitude reduction factor was set to 0.7 for all the samples.

The E_0 value was refined for one of the samples and found equal to 1.5 eV. It was kept fixed to this value for the rest of the samples. We performed the fits by fixing the coordination numbers to the crystallographic values for bcc Fe (8 for the NN atoms and 6 for the NNN neighbors) and letting the Ga population vary together with the Debye-Waller factors and interatomic distances. The variation of the interatomic distances was limited in a range physically reasonable according to our previous results on the same system.

More details about the EXAFS analysis are given in a previous Galfenol paper dealing with the same kind of samples [39]. Figure 3c displays an example of the best-fit curves in R-space for the two polarizations for one of the samples presented here. The overall results are reported in Table 2.

All the samples show the same local environment around the Ga absorber at the Ga K-edge, independent of Ga concentration and sample thickness: no gallium atoms are found in the NN and NNN of the Ga absorber. That is expected for a D0₃-like ordering at a local scale and excludes the mD0₃ structure. When we look at the Fe environment, by performing EXAFS at the Fe K-edge, we found a population of Ga scatterers, in

the NN coordination shell close to 30% for the 22% concentration, and close to 50% for the 28% and 33% Ga samples. No Ga atoms are found in the NNN shell. This is in agreement with what is observed at the Ga K-edge, i.e., the general and expected tendency of the Ga atoms to stay apart from each other at the local scale [39]. Short-range D0₃ ordering occurs, in which 50% of the NN are Ga atoms and no Ga NNN are expected. We have to note that the precision in determining composition by EXAFS is not very high, and we cannot exclude the presence of Ga as a scatterer below values of up to 10% in atomic composition. The interatomic distances of the first shell are determined for Ga-Fe (Ga threshold), Fe-Ga (Fe threshold), and Fe-Fe (Fe threshold), and exhibit a bimodal distribution. The Fe-Fe distance is equal to the bulk Fe value, while the Ga-Fe distance is around 2.52 Å, as previously observed in the literature [48]. The determination of the interatomic distances of the second shell is more challenging and less precise. Diffraction measurements provide the value of the lattice parameter in the direction perpendicular to the surface, which is used in the fits to determine the in-plane lattice parameter. A slight distortion is observed in the samples with $x = 22$ and 28, and a somewhat higher distortion in the $x = 33$ samples. An important increase in the structural disorder is observed as the Ga content increases, both in the Ga and Fe environments. No structural changes are observed as the sample thickness increases.

3.3. XANES Results

We have also studied the near-edge region of the XAFS spectra, which is known to be sensitive to small changes in the geometry of the absorber environment. The Ga-Ga pairs presence has been addressed in previous papers by analyzing the Linear Dichroism signal in the XANES spectra at the Ga K-edge [33, 49]. XANES is more sensitive than EXAFS to local geometrical distortions which gives rise to anisotropy. The XANES raw spectra recorded with in-plane and out-of-plane polarization were normalized to each other in the post-edge extended region and the LD Xanes signals were calculated as $\mu_{LD} = \mu_{||} - \mu_{\perp}$. They are shown in Fig. 4a for the samples studied with the exception of samples 28-11 and 33-36, the spectra of which did not have enough quality to perform this analysis. A dichroic signal of the same type is observed in all the samples, as expected due to the distortion of the cubic cell. The LD signal is more intense for the samples with 21% Ga, which do not show a SL diffraction peak. On the other hand, according to EXAFS, they are characterized by a more ordered local environment than the richer Ga samples. The observed μ_{LD} agree with a previous paper reporting on the origin of magnetic anisotropy of Ga-rich FeGa films grown by sputtering with different thicknesses[49]. In that study, a feature was observed that could be ascribed to the formation of Ga-Ga pairs only for thicknesses above 100 nm. Our samples are thinner than 50 nm and do not show such a feature. A qualitative interpretation of the XANES spectra can be provided by performing *ab initio* simulations and comparing the overall theoretical spectrum with the experiment. We used the FDMNES code [50] for *ab initio* calculation of the X-ray absorption threshold in the two

Sample	x_I		x_{II}		σ_I^2 ($\text{\AA}^2 \times 10^{-3}$)		σ_{II}^2 ($\text{\AA}^2 \times 10^{-3}$)		d_I (\AA)		$d_{II\parallel}$ (\AA)		$d_{II\perp}$ (\AA)
	K-Ga	K-Fe	K-Ga	K-Fe	K-Ga	K-Fe	K-Ga	K-Fe	(Ga-Fe)	(Fe-Ga)	(Ga-Fe)	(Fe-Ga(Fe))	(diff)
22-10	0.0(1)	0.32(7)	0.0	0.0	7(1)	4.5(6)	16(2)	16(3)	2.52(1)	2.53(2)	2.87(1)	2.89(2)	2.89
22-33	0.0(1)	0.36(6)	0.0	0.0	7(1)	5(1)	19(2)	15(3)	2.52(1)	2.53(2)	2.87(1)	2.87(2)	2.89
28-11	0.0(1)	0.47(4)	0.0	0.0	10(1)	6(1)	27(1)	30(6)	2.52(1)	2.53(2)	2.87(1)	2.87(2)	2.89
28-41	0.0(2)	0.56(4)	0.0	0.0	8(1)	7(1)	28(1)	38(8)	2.51(1)	2.53(1)	2.90(1)	2.87(3)	2.89
33-13	0.0(2)	0.56(4)	0.0	0.0	9(1)	6(1)	30(9)	44(15)	2.53(1)	2.53(1)	2.89(1)	2.88(4)	2.91
33-25	0.1(2)	0.51(4)	0.0	0.0	9(1)	6(1)	27(9)	32(7)	2.50(1)	2.53(3)	2.87(2)	2.89(3)	2.91
33-36	0.0(2)	0.56(4)	-	-	10(1)	7(1)	40(12)	39(9)	2.52(1)	2.53(1)	2.87(1)	2.87(3)	2.91

Table 2: Best fit results for the studied samples at the Ga and Fe K-edges. The perpendicular and parallel polarization spectra were fitted simultaneously. We report the fit parameters as Ga population I and II shells (x_I and x_{II}), Debye-Waller factors, interatomic distances of I coordination shell, d_I , and II coordination shells, in-plane $d_{II\parallel}$, and out-of-plane, $d_{II\perp}$. The statistical errors, given in parenthesis, were calculated from the diagonal values of the fit covariance matrix. The errors on x_{II} are all about 0.1. The interatomic out-of-plane distance values for the II coordination shell were kept fixed to the values found by diffraction.

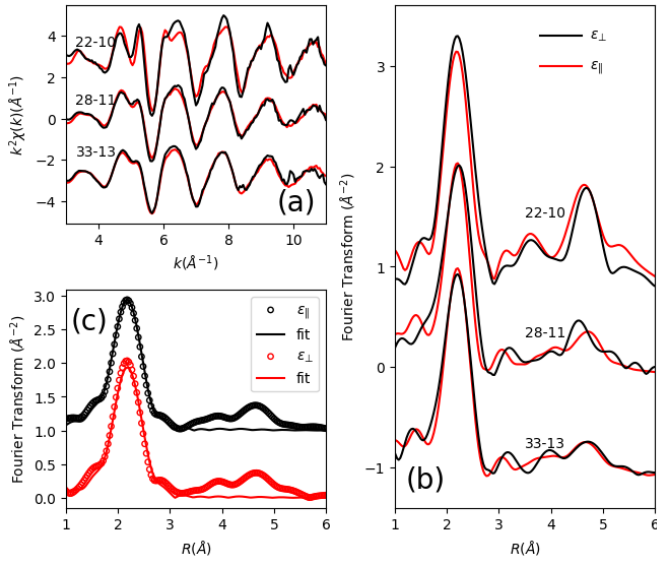


Figure 3: a) Raw background subtracted EXAFS spectra and b) correspondent Fourier Transform amplitudes at the Ga K-edge, of some of the samples studied with close to in-plane (red line) and out-of-plane (black line) polarization of the incoming beam. An example of best-fit results is given in panel c), showing FT amplitudes of the EXAFS signal (circles) for the two X-ray beam polarization directions, for one of the samples (33-13) together with the corresponding best-fit curves (solid lines). Fits were performed in q-space.

polarization directions and the correspondent μ_{LD} . The simulations were performed for an FeGa cluster with D0₃ (25 % Ga) and B2 (50 % Ga) ordering. A 1% distortion of the crystal lattice was applied while keeping the cell volume constant. We verified that the calculation converges for a 9 \AA cluster. The results are shown in Figure 4b, where we compare one of the experimental XANES spectra with the theoretical XANES for the two models, and in Figure 4c, in which we compare experimental and theoretical μ_{LD} . The theoretical XANES spectra qualitatively reproduce the experimental spectra, which appear to have a shape between the D0₃ and B2 structure calculations.

The XANES results are consistent with the EXAFS results, showing the tendency of Ga atoms to be apart from each other but without excluding the presence of a low number of Ga-Ga pairs. If we compare the μ_{LD} of the whole sample set, we can observe a clear lowering of the μ_{LD} intensity when increasing

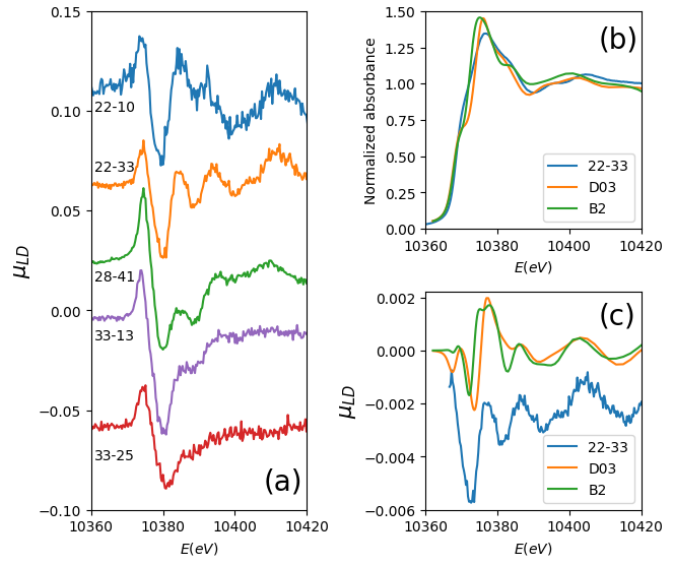


Figure 4: a) LD-XANES spectra at the Ga K-edge, obtained by subtraction of in-plane and out-of-plane polarized XANES spectra for the studied samples. b) XANES spectra, with in-plane polarization, for sample 22-33 (blue curve) are compared with two *ab initio* simulations, performed by the FDMNES code, for two clusters with 9 \AA radius, having D0₃ (yellow curve) and B2 (green curve) symmetry. c) LD-XANES signal for sample 22-33 compared with the two simulations, D0₃ (yellow curve) and B2 (green curve).

the Ga content. This can be associated with the increasing local disorder observed by EXAFS. It could, in turn, favor the formation of pairs, which, even in small numbers, can modulate the magnetic behavior of the system.

3.4. Magnetic anisotropy

Figure 5 displays hysteresis loops obtained by MOKE, with the signal normalized to the saturation value, and $\mu_0 H$ applied along the [100] and [110] axis. It illustrates the behavior of the three compositions presented here comparing a reference Fe film and sample 22-19. Thus, for the pure iron films, the easy direction (EA) is the $\langle 100 \rangle$ axes, while for the FeGa films, the EA shifts to the $\langle 110 \rangle$ in-plane direction. $K_1 \approx -16 \text{ kJm}^{-3}$ for the 22-19 film, $M_s \approx 1.45 \text{ T}$ and around 30 kJm^{-3} for a reference Fe film, $M_s \approx 2.08 \text{ T}$ [51].

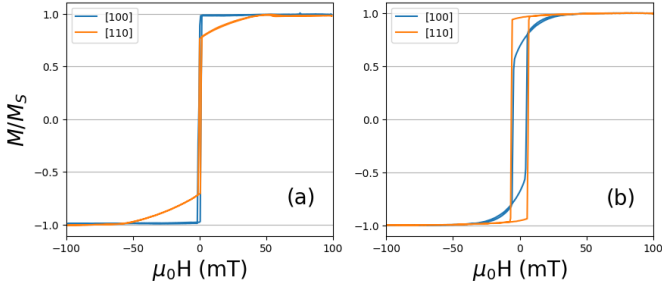


Figure 5: M-H loops with H along the [100] and [110] directions for (a) Fe film and (b) 22-19 film.

3.5. Magnetoelastic stresses

Figure 6a-f shows sets of ME stress curves for samples of the three compositions presented in this work. For the thinner films, around 10 nm, they present jumps due to the lower signal-noise ratio, which is proportional to the film volume. The shape of these curves reflects the in-plane easy axis orientation [110], with a saw and parabolic features when the hard and easy axis are along the cantilever beam. It is noted that the films are saturated at 100 mT as is shown in Fig. 5.

The thickness dependence of B_1 and B_2 is displayed in Figure 6 g and h. The variation of values is minute and within the experimental error, including composition fluctuation. The latter may be more relevant for B_2 the $x = 22$ series since it changes sign around this composition. The largest value of $-B_1 \sim 10$ MPa in those sets of films is observed for $x = 22$ and decreases to $-B_1 \sim 6$ MPa for higher concentrations of Ga. B_1 , in modulus, is larger for all compositions than that reported for Fe bulk ($-B_1 = 3.44$ MPa). The highest value is obtained for a film with 17-48, 12 MPa, the composition where the first peak of $\lambda_{100}(x)$ takes place. Interestingly, $-B_1 \sim 10$ MPa obtained in the films with $x \approx 22$ is about two times larger than the bulk value, about 5 MPa, calculated from the $(3/2)\lambda_{100} = 200 \cdot 10^{-6}$ and $c_{11} - c_{12} = 25.2$ GPa [51]. Above that composition, $-B_1$ obtained here take similar values to the bulk ones, where $-B_1 = 6.5$ MPa for $x=28.8$ and 9 MPa for $x=35.2$ [51]. EXAFS results, with spectra taken at the Ga K-edge support the absence of local ordering or a significant pairs between the reference Ga atoms and the positions at neighbor first of second layers, with a minute presence of Ga-Ga NNN pairs. The presence of some Ga-Ga pairs is suggested qualitatively by the analysis of μ_{LD} by introducing the B2 phase in the environment of the Ga atom.

Because of the strong link between crystal structure and magnetoelastic stress in FeGa alloys [23, 43], we note that the enhancement of B_1 is observed with the absence of SL peaks in x-ray experiments, see Figure 1.d where the (001) reflection does not appear for the 22-19 film indicating that only the A2 phase is formed in the film. For the $x = 28$ and 33 compositions, the (001) peak is displayed. Therefore, this experimental fact points to values for B_1 in films with the A2 crystal structure that multiply by 2 the bulk value. The direct observation of a large value of $-B_1$ in films with A2 structure agrees with the observation obtained in films grown on PMN-PT, where a significant increment of $-B_1 \approx 18$ MPa was obtained by the measurement

of magnetic anisotropy constant [5]. *Ab initio* calculations with the quasirandom-structure method to face disordered supercells [21], support the enhancement of $-B_1 (=8.7$ MPa) with respect to Fe calculated value ($=5.1$ MPa) by the presence of random Ga atoms in an A2 structure with $x=18.75$. That increment for $-B_1$ is larger if Ga-Ga pairs are introduced in the calculation with the mD0₃ structure ($=19.2$ MPa). In bulk samples, the preparation procedure involves the coexistence of A2 and other phases, with a proportion that depends on the recipe used. The preparation method for flat thin films, growth at a substrate temperature of 150 °C, and low flux of materials may retard the formation of a more ordered phase in favor of the disordered A2 structure.

B_2 is smaller, in modulus, than the corresponding bulk values [51] obtained for the film studied here, including the Fe film. Thus, bulk values are -12 MPa for $x = 28$ and -9.2 MPa for $x = 33$, while thin films are roughly forty percent of the bulk for those compositions. On the other hand, for $x = 22$, B_2 is positive while the bulk value is negative, indicating that the switch of the sign of B_2 is shifted toward higher x values due to the persistence of the A2 structure in the thin films.

Another observation regarding B_1 and B_2 in FeGa films is the lack of significant effects associated with film thickness, contrasting with the behavior reported for Fe films. This result may agree with the conclusion obtained from the fully relativistic disordered local moment theory applied to fully disordered FeGa alloys [19]. In this study, increasing the Ga content reduces the volume sensitivity of B_1 calculated for pure iron, becoming it negligible for $x = 20$, although the same calculation does not show enhancement of B_1 for disordered A2 FeGa alloys.

Finally, we hypothesize about the role of the intrinsic deformation of the A2 phase. The lattice parameters data indicate that the films undergo a tetragonal distortion with the enlarged azimuthal plane. Extrinsic mechanisms require the rotation of the strained A2 phase with local distortions by nanoparticles with Ga-Ga pairs along the magnetic field [12], so only mD0₃ particles within-plane Ga-Ga pairs would contribute with $\mu_0 H$ rotating in the film plane. However, the distortion of these particles and the A2 matrix is affected and controlled by the substrate, which promotes lattice parameters either with homogeneous deformation or, above a certain critical thickness, a relaxation by generating misfit dislocations. Therefore, local internal stresses can be large because they are proportional to the difference between actual and unconstrained lattice parameters, but tied to the substrate. Thus, the substrate would freeze the displacement of the induced deformation in the A2 structure by uniaxial particles, and only the distortion generated by the spin-orbit effect remains. It is noticeable that even in films with SL peaks, synchrotron X-ray diffraction, and EXAFS discard the presence of uniaxial particles in significant proportions.

4. Summary

In this article, the tetragonal and rhombohedral magnetoelastic coupling coefficients are obtained in epitaxial thin films as a function of composition and thickness using a cantilever

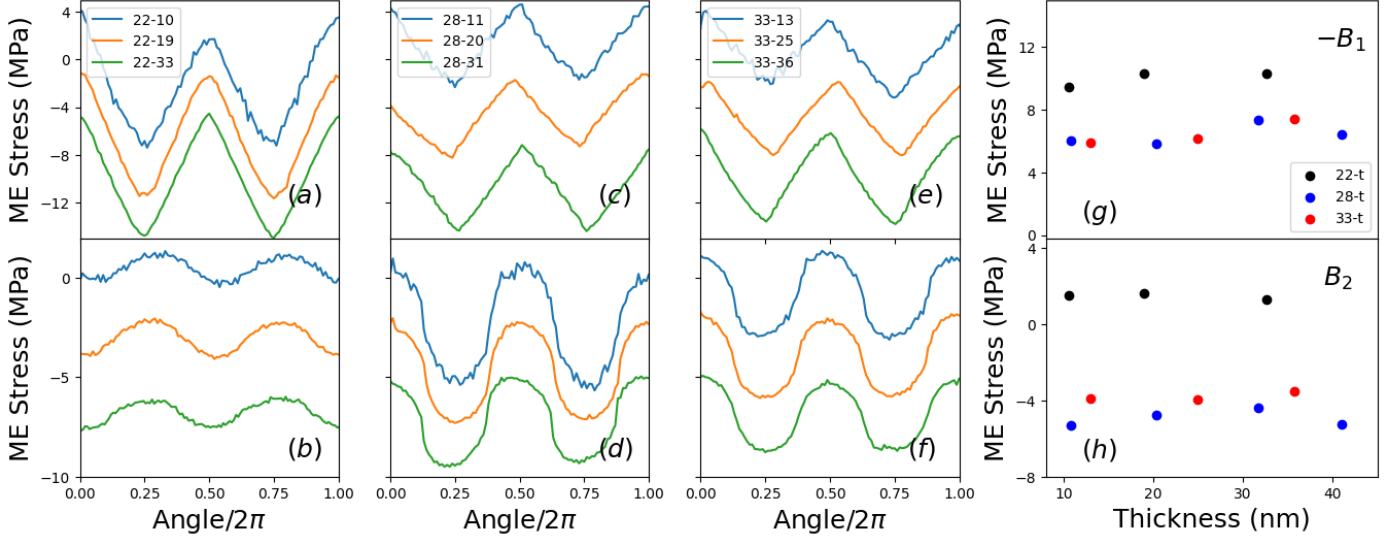


Figure 6: Magnetoelastic stress measurements vs angle (a)-(f) for films with $x = 22$ (a) and (b), $x = 28$ (c) and (d) $x = 33$ (e) and (f). The angle = 0 position is set with $\mu_0 H \parallel$ beam length. Panels (a), (c), and (e) show measurements performed in films with beams along the FeGa[100] direction to determine B_1 . For panels (b), (d), and (f) beams is parallel to FeGa[110] obtaining B_2 . Stress curves are shifted along the y-axis for clarity purposes. Thickness dependencies for the (g) $-B_1$ and (h) B_2 ME coefficients.

method. We show the enhancement of $-B_1 \approx 10$ MPa in thin films with A2 structure, at the composition with $x = 22$, which presents the DO_3 precipitates in bulk samples, doubling that bulk value. The direct observation of a significant value of $-B_1$ in films with A2 structure jibes with B_1 obtained through the measurement of the modification magnetic anisotropy constant with strain in films grown on ferroelectric PMN-PT substrates [5]. The enhancement of $-B_1$ due to the presence of random Ga atoms in an A2 structure ($x=18.75$) is also supported by *ab initio* calculations with the quasirandom-structure method to face disordered supercells [21] being that increment larger if Ga-Ga pairs are introduced in the calculation (m DO_3 structure).

The dependence of B_1 and B_2 with the film thickness does not show variations associated with that parameter. In addition, $-B_1$ has a maximum for $x=17$ and decreases for any compositions with higher content of Ga. Regarding B_2 , smaller values than bulk values are obtained for the films studied here, including the Fe film. The switch of the sign of B_2 in the films is shifted toward higher x values due to the persistence of the A2 structure.

Thus, we suggest that the strain induced by the substrate in combination with the *low-temperature* growth conditions hinder the formation of ordered species of the FeGa alloy (DO_3 , m DO_3 , B2, etc.) observed or proposed in bulk samples, with the interesting result of the enlarging B_1 by a factor 2 compared to the bulk value for $x = 22$. Therefore, taking $K_1/4 \approx 4 \text{ kJm}^{-3}$ for the 22-19 film, the condition $B_1 \epsilon > K_1/4$ to control energy minima with strain switching may require $|\epsilon|$ as low as $0.4 \cdot 10^{-3}$ to revert the sign of the uniaxial anisotropy and reduce the strength of external stimuli related to ϵ applied to magnetic devices placed at the central gap of electrode pairs on ferroelectric substrates [52]. Therefore, we showed that the epitaxy of FeGa with large ME stress and low magnetoelastic anisotropy

can be obtained in thin films with low roughness without needing high-temperature treatments.

FeGa and other heterostructured materials open the door to improve magnetoelastic performance by several mechanisms that can be complementary to each other; one is the modification of electronic structure and the activation of soft phases by inclusions and nanoprecipitates. From a practical point of view, these short-range interactions boost the magnetoelastic stress and diminish the magnetic anisotropy with applications at low fields and malleable magnetic anisotropy by applying external strain. In conclusion, we infer that the strength of the electronic effects of *bcc* iron alloys is worth exploring and suggest the relevance of the modifications of the iron atom electronic structure by alloying with gallium.

5. CRediT authorship contribution statement

Adrian Begué: data curation, formal analysis, investigation, validation, writing - review & editing. **Maria Grazia Proietti:** data curation, formal analysis, visualization investigation, validation, writing - review & editing, funding acquisition. **José Ignacio Arnaudas:** formal analysis, writing - review & editing, funding acquisition. **Miguel Ciria:** data curation, validation, investigation, formal analysis, visualization, funding acquisition, writing – original draft.

6. Acknowledgments

We thanks grant TED2021-131064B-I00 funded by MCIN/AEI/10.13039/501100011033 and by European Union NextGenerationEU/PRTR, grant PID2021-124734OB-C21 funded by MCIN/AEI/10.13039/501100011033 and by “ERDF A way of making Europe” and grant CEX2023-001286-S funded

by MICIU/AEI/10.13039/501100011033 and Gobierno de Aragón (grant E12-23R). A. B. would like to acknowledge the funding received from the Ministry of Universities and the European Union-Next Generation for the Margarita Salas fellowship. We are grateful to the staff of beamline B18 at Diamond UK's National Synchrotron Light source and BM25 Spain Beamline at ESRF for their strong support in performing the experiments. Authors would like to acknowledge the use of Servicio General de Apoyo a la Investigación-SAI, Universidad de Zaragoza. Authors acknowledge the use of instrumentation as well as the technical advice provided by the National Facility ELECMI ICTS, node Laboratorio de Microscopias Avanzadas (LMA) at Universidad de Zaragoza.

7. Bibliography

References

- [1] A. E. Clark, M. Wun-Fogle, J. Restorff, T. Lograsso, J. Cullen, Effect of quenching on the magnetostriction on $\text{Fe}_{1-x}\text{Ga}_x$ ($0.13 < x < 0.21$), *IEEE Trans. Magn.* 37 (4) (2001) 2678–2680. doi:10.1109/20.951272.
- [2] A. E. Clark, K. B. Hathaway, M. Wun-Fogle, J. B. Restorff, T. A. Lograsso, V. M. Keppens, G. Petculescu, R. A. Taylor, Extraordinary magnetoelasticity and lattice softening in bcc Fe-Ga alloys, *J. Appl. Phys.* 93 (10 3) (2003) 8621–8623. doi:10.1063/1.1540130.
- [3] S. Rafique, J. R. Cullen, M. Wuttig, J. Cui, Magnetic anisotropy of FeGa alloys, *J. Appl. Phys.* 95 (11 II) (2004) 6939–6941. doi:10.1063/1.1676054.
- [4] A. Begué, M. Ciria, Strain-mediated giant magnetoelectric coupling in a crystalline multiferroic heterostructure, *ACS Appl. Mater. Interfaces* 13 (5) (2021) 6778–6784. doi:10.1021/acsmami.0c18777.
- [5] P. B. Meisenheimer, R. A. Steinhart, S. H. Sung, L. D. Williams, S. Zhuang, M. E. Nowakowski, S. Novakov, M. M. Torunbalci, B. Prasad, C. J. Zollner, Z. Wang, N. M. Dawley, J. Schubert, A. H. Hunter, S. Manapatruni, D. E. Nikonov, I. A. Young, L. Q. Chen, J. Bokor, S. A. Bhavé, R. Ramesh, J.-M. Hu, E. Kioupakis, R. Hovden, D. G. Schlom, J. T. Heron, Engineering new limits to magnetostriction through metastability in iron-gallium alloys, *Nat Commun* 12 (1) (2021) 2757. doi:10.1038/s41467-021-22793-x.
- [6] J.-M. Hu, C.-W. Nan, Opportunities and challenges for magnetoelectric devices, *APL Materials* 7 (8) (2019) 080905. doi:10.1063/1.5112089.
- [7] K. Yang, A. Sengupta, Stochastic magnetoelectric neuron for temporal information encoding, *Appl. Phys. Lett.* 116 (4) (2020) 043701. doi:10.1063/1.5138951.
- [8] A. Sakai, S. Minami, T. Koretsune, T. Chen, T. Higo, Y. Wang, T. Nomoto, M. Hirayama, S. Miwa, D. Nishio-Hamane, F. Ishii, R. Arita, S. Nakatsuji, Iron-based binary ferromagnets for transverse thermoelectric conversion, *Nature* 581 (7806) (2020) 53–57. doi:10.1038/s41586-020-2230-z.
- [9] Z. Feng, S. Minami, S. Akamatsu, A. Sakai, T. Chen, D. Nishio-Hamane, S. Nakatsuji, Giant and robust anomalous nernst effect in a polycrystalline topological ferromagnet at room temperature, *Adv. Funct. Mater.* 32 (49) (2022) 2206519. doi:10.1002/adfm.202206519.
- [10] J. Boisse, H. Zapolsky, A. G. Khachatryan, Atomic-scale modeling of nanostructure formation in Fe-Ga alloys with giant magnetostriction: Cascade ordering and decomposition, *Acta Mater.* 59 (7) (2011) 2656–2668. doi:10.1016/j.actamat.2011.01.002.
- [11] V. Palacheva, A. Emdadi, F. Emeis, I. Bobrikov, A. Balagurov, S. Divinski, G. Wilde, I. Golovin, Phase transitions as a tool for tailoring magnetostriction in intrinsic Fe-Ga composites, *Acta Mater.* 130 (2017) 229–239. doi:10.1016/j.actamat.2017.03.049.
- [12] H. Yangkun, K. Xiaoqin, J. Chengbao, M. Naihua, W. Hui, C. J. M. David, W. Yunzhi, X. Huibin, Interaction of Trace Rare-Earth Dopants and Nanoheterogeneities Induces Giant Magnetostriction in Fe-Ga Alloys, *Adv Funct Mater* 28 (20) (2018) 1800858. doi:10.1002/adfm.201800858.
- [13] C. Zhang, J. Gou, J. Yang, T. Ma, L. Sun, G. Sun, Q. Tian, G. Yan, L. Chen, P. Zhang, Y. Liu, Nanoheterogeneity response in large-magnetostriction Fe-Ga alloys: An in-situ magnetic small-angle neutron scattering study, *Acta Mater.* 225 (2022) 117594. doi:10.1016/j.actamat.2021.117594.
- [14] K. Yan, Y. Xu, J. Niu, Y. Wu, Y. Li, B. Gault, S. Zhao, X. Wang, Y. Li, J. Wang, K. P. Skokov, O. Gutfleisch, H. Wu, D. Jiang, Y. He, C. Jiang, Unraveling the origin of local chemical ordering in Fe-based solid-solutions, *Acta Mater.* 264 (2024) 119583. doi:10.1016/j.actamat.2023.119583.
- [15] Y. He, C. Jiang, W. Wu, B. Wang, H. Duan, H. Wang, T. Zhang, J. Wang, J. Liu, Z. Zhang, P. Stamenov, J. Coey, H. Xu, Giant heterogeneous magnetostriction in Fe-Ga alloys: Effect of trace element doping, *Acta Mater.* 109 (2016) 177–186. doi:10.1016/j.actamat.2016.02.056.
- [16] H. Wang, Y. N. Zhang, T. Yang, Z. D. Zhang, L. Z. Sun, R. Q. Wu, Ab initio studies of the effect of nanoclusters on magnetostriction of $\text{Fe}_{1-x}\text{Ga}_x$ alloys, *Appl. Phys. Lett.* 97 (26) (2010) 262505. doi:10.1063/1.3533659.
- [17] H. Wang, Y. N. Wu, R. Q. Sun, L. Z. Xu, D. S., Z. D. Zhang, Understanding strong magnetostriction in $\text{Fe}_{100-x}\text{Ga}_x$ alloys, *Sci. Rep.* 3 (2013) 3521. doi:10.1038/srep03521.
- [18] G. A. Marchant, C. D. Woodgate, C. E. Patrick, J. B. Staunton, Ab initio calculations of the phase behavior and subsequent magnetostriction of $\text{Fe}_{1-x}\text{Ga}_x$ within the disordered local moment picture, *Phys. Rev. B* 103 (2021) 094414. doi:10.1103/PhysRevB.103.094414.
- [19] G. A. Marchant, C. E. Patrick, J. B. Staunton, Ab initio calculations of temperature-dependent magnetostriction of Fe and Al $\text{Fe}_{1-x}\text{Ga}_x$ within the disordered local moment picture, *Phys. Rev. B* 99 (2019) 054415. doi:10.1103/PhysRevB.99.054415.
- [20] M. Adelani, S. F. Olive-Méndez, F. Espinosa-Magaña, J. A. Matutes-Aquino, M. Grijalva-Castillo, Structural, magnetic and electronic properties of Fe-Ga-Tb_x ($0 \leq x \leq 1.85$) alloys: Density-functional theory study, *J. Alloys Compd.* 857 (2021) 157540. doi:10.1016/j.jallcom.2020.157540.
- [21] J. Niu, K. Yan, Y. Xu, Y. Wu, E. Liu, Z. Fu, J. Li, X. Gao, X. Mu, B. Liu, X. Wang, Y. Li, J. Wang, C. Jiang, Understanding the intrinsic mechanism of the giant magnetostriction in binary and alloyed FeGa solid solutions, *Phys. Rev. B* 109 (2024) 014417. doi:10.1103/PhysRevB.109.014417.
- [22] W.-F. Rao, M. Wuttig, A. G. Khachatryan, Giant nonhysteretic responses of two-phase nanostructured alloys, *Phys. Rev. Lett.* 106 (2011) 105703. doi:10.1103/PhysRevLett.106.105703.
- [23] Q. Xing, Y. Du, R. J. McQueeney, T. a. Lograsso, Structural investigations of Fe-Ga alloys: Phase relations and magnetostrictive behavior, *Acta Mater.* 56 (16) (2008) 4536–4546. doi:10.1016/j.actamat.2008.05.011.
- [24] A. M. Balagurov, I. A. Bobrikov, D. Y. Chernyshov, A. S. Sohatsky, S. V. Sumnikov, B. Yerzhanov, I. S. Golovin, Tetragonal phases in Fe-Ga alloys: A quantitative study, *Phys. Rev. Mater.* 8 (2024) 073604. doi:10.1103/PhysRevMaterials.8.073604.
- [25] J. Gou, T. Ma, X. Liu, C. Zhang, L. Sun, G. Sun, W. Xia, X. Ren, Large and sensitive magnetostriction in ferromagnetic composites with nanodispersive precipitates, *NPG Asia Materials* 13 (2021) 6. doi:10.1038/s41427-020-00276-7.
- [26] A. Begué, M. G. Proietti, J. I. Arnaudus, M. Ciria, Magnetic ripple domain structure in FeGa/MgO thin films, *J. Magn. Magn. Mater.* 498 (2020) 166135. doi:10.1016/j.jmmm.2019.166135.
- [27] A. E. Clark, M. Wun-Fogle, J. B. Restorff, K. W. Dennis, T. A. Lograsso, R. W. McCallum, Temperature dependence of the magnetic anisotropy and magnetostriction of $\text{Fe}_{100-x}\text{Ga}_x$ ($x=8.6, 16.6, 28.5$), *J. Appl. Phys.* 97 (10) (2005) 10M316. doi:10.1063/1.1856731.
- [28] M. Barturen, D. Sander, J. Milano, J. Prempere, C. Helman, M. Eddrief, J. Kirschner, M. Marangolo, Bulklike behavior of magnetoelasticity in epitaxial $\text{Fe}_{1-x}\text{Ga}_x$ thin films, *Phys. Rev. B* 99 (2019) 134432. doi:10.1103/PhysRevB.99.134432.
- [29] E. du Tremolet de Lacheisserie, R. Mendia Monterroso, Magnetostriction of iron, *J. Magn. Magn. Mater.* 31-34 (1983) 837–838. doi:10.1016/0304-8853(83)90704-7.
- [30] S. Soriano, C. Dufour, K. Dumesnil, J. A. Borchers, P. Mangin, Clamping effects in the $\text{Al}_2\text{O}_3(112-0)/\text{Nb}(110)/\text{Eu}(110)$ epitaxial system, *Appl. Phys. Lett.* 85 (20) (2004) 4636–4638. doi:10.1063/1.1821658.

- [31] A. Javed, N. A. Morley, M. R. J. Gibbs, Thickness dependence of magnetic and structural properties in $\text{Fe}_{80}\text{Ga}_{20}$ thin films, *J. Appl. Phys.* 107 (9) (2010) 09A944. doi:10.1063/1.3368107.
- [32] M. Jiménez, G. Cabeza, J. Gámez, D. Velázquez Rodríguez, L. Leiva, J. Milano, A. Butera, Thickness dependence of the magnetoelectric coupling in $\text{Fe}_{89}\text{Ga}_{11}$ thin films deposited on ferroelectric PMN-PT single crystals, *J. Magn. Magn. Mater.* 501 (2020) 166361. doi:10.1016/j.jmmm.2019.166361.
- [33] P. Bartolomé, A. Begué, A. Muñoz-Noval, M. Ciria, R. Ranchal, Unveiling the Different Physical Origins of Magnetic Anisotropy and Magnetoelasticity in Ga-Rich FeGa Thin Films, *J. Phys. Chem. C* 124 (8) (2020) 4717–4722. doi:10.1021/acs.jpcc.9b10879.
- [34] W. Jahjah, R. Manach, Y. Le Grand, A. Fessant, B. Warot-Fonrose, A. Prinsloo, C. Sheppard, D. Dekadjevi, D. Spenato, J.-P. Jay, Thickness dependence of magnetization reversal and magnetostriction in $\text{Fe}_{81}\text{Ga}_{19}$ thin films, *Phys. Rev. Appl.* 12 (2019) 024020. doi:10.1103/PhysRevApplied.12.024020.
- [35] G. A. Ramírez, A. E. M. Rizzo, J. E. Gómez, D. Goijman, L. M. Rodríguez, D. Fregenal, A. Butera, J. Milano, Magnetoelasticity of $\text{Fe}_{1-x}\text{Ga}_x$ thin films on amorphous substrates, *Phys. Rev. B* 104 (2021) 064403. doi:10.1103/PhysRevB.104.064403.
- [36] L. Dominguez, K. Kulakowski, Model calculations of the magnetoelastic coefficient $b^{\gamma-2}$ in crystalline iron, *J. Magn. Magn. Mater.* 185 (1) (1998) 121–126. doi:10.1016/S0304-8853(98)00020-1.
- [37] R. Koch, M. Weber, K. Thürmer, K. H. Rieder, Magnetoelastic coupling of Fe at high stress investigated by means of epitaxial Fe(001) films, *J. Magn. Magn. Mater.* 159 (1) (1996) L11–L16. doi:10.1016/0304-8853(96)00291-0.
- [38] G. Wedler, J. Walz, A. Greuer, R. Koch, The magnetoelastic coupling constant B_2 of epitaxial Fe(001) films, *Surf. Sci.* 454-456 (2000) 896–899. doi:10.1016/S0039-6028(00)00104-7.
- [39] M. Ciria, M. G. Proietti, E. C. Corredor, D. Coffey, A. Begué, C. de la Fuente, J. I. Arnaudas, A. Ibarra, Crystal structure and local ordering in epitaxial $\text{Fe}_{100-x}\text{Ga}_x/\text{MgO}(001)$ films, *J. Alloys Compd* 767 (2018) 905–914. doi:10.1016/j.jallcom.2018.07.120.
- [40] D. Lahiri, XAFS characterization of materials—a realistic evaluation, *Handbook of Materials Science I* (2024) 597–637. doi:10.1007/978-981-99-7145-9_20.
- [41] F. de Groot, J. Vogel, Fundamentals of x-ray absorption and dichroism: the multiplet approach, in: *Neutron and X-ray Spectroscopy*, Springer, pp. 3–66.
- [42] N. Kawamiya, K. Adachi, Y. Nakamura, Magnetic Properties and Mössbauer Investigations of Fe-Ga Alloys, *J. Phys. Soc. Jpn.* 33 (5) (1972) 1318–1327. doi:10.1143/JPSJ.33.1318.
- [43] Y. Du, M. Huang, S. Chang, D. L. Schlagel, T. A. Lograsso, R. J. McQueeney, Relation between Ga ordering and magnetostriction of Fe-Ga alloys studied by x-ray diffuse scattering, *Phys. Rev. B* 81 (5) (2010) 1–9. doi:10.1103/PhysRevB.81.054432.
- [44] C. Guillemard, S. Petit-Watelot, T. Devolder, L. Pasquier, P. Boulet, S. Migot, J. Ghanbaja, F. Bertran, S. Andrieu, Issues in growing heusler compounds in thin films for spintronic applications, *J. Appl. Phys.* 128 (24) (2020) 241102. doi:10.1063/5.0014241.
- [45] B. Ravel, ATOMS: crystallography for the X-ray absorption spectroscopist, *J. Synchrotron Rad.* 8 (2001) 314–316. doi:10.1107/S090904950001493X.
- [46] A. L. Ankudinov, B. Ravel, J. J. Rehr, S. D. Conradson, Real-space multiple-scattering calculation and interpretation of X-ray-absorption near-edge structure, *Phys. Rev. B* 58 (12) (1998) 7565–7576. doi:10.1103/PhysRevB.58.7565.
- [47] B. Ravel, M. Newville, ATHENA, ARTEMIS, HEPHAESTUS: data analysis for X-ray absorption spectroscopy using IFEFFIT, *J. Synchrotron Rad.* 12 (4) (2005) 537–541. doi:10.1107/S0909049505012719.
- [48] S. Pascarelli, M. Ruffoni, R. Sato Turtelli, F. Kubel, R. Grössinger, Local structure in magnetostrictive melt-spun $\text{Fe}_{80}\text{Ga}_{20}$ alloys, *Phys. Rev. B* 77 (18) (2008) 1–8. doi:10.1103/PhysRevB.77.184406.
- [49] A. Muñoz-Noval, S. Fin, E. Salas-Colera, D. Bisero, R. Ranchal, The role of surface to bulk ratio on the development of magnetic anisotropy in high Ga content $\text{Fe}_{100-x}\text{Ga}_x$ thin films, *J. Alloys Compd* 745 (2018) 413–420. doi:10.1016/j.jallcom.2018.02.223.
- [50] O. Bunau, Y. Joly, Self-consistent aspects of x-ray absorption calculations, *J. Phys.: Condens. Matter* 21 (2009) 345501. doi:10.1088/0953-8984/21/34/345501.
- [51] J. B. Restorff, M. Wun-Fogle, K. B. Hathaway, A. E. Clark, T. A. Lograsso, G. Petculescu, Tetragonal magnetostriction and magnetoelastic coupling in Fe-Al, Fe-Ga, Fe-Ge, Fe-Si, Fe-Ga-Al, and Fe-Ga-Ge alloys, *J. Appl. Phys.* 111 (2) (2012) 023905. doi:10.1063/1.3674318.
- [52] A. Chen, Y. Zhao, Y. Wen, L. Pan, P. Li, X.-X. Zhang, Full voltage manipulation of the resistance of a magnetic tunnel junction, *Sci. Adv.* 5 (12) (2019). doi:10.1126/sciadv.aay5141.
- [53] P. Marcus, Magnetostrictive bending of a cantilevered film-substrate system, *J. Magn. Magn. Mater.* 168 (1) (1997) 18–24. doi:10.1016/S0304-8853(96)00691-9.
- [54] E. du Trémolet de Lacheisserie, J. Peuzin, Magnetostriction and internal stresses in thin films: the cantilever method revisited, *Journal of Magnetism and Magnetic Materials* 136 (1) (1994) 189–196. doi:10.1016/0304-8853(94)90464-2.
- [55] V. Iannotti, L. Lanotte, Improved model for the magnetostrictive deflection of a clamped film-substrate system, *J. Magn. Magn. Mater.* 202 (1) (1999) 191–196. doi:10.1016/S0304-8853(99)00330-3.
- [56] R. Watts, M. R. J. Gibbs, W. J. Karl, H. Szymczak, Finite-element modelling of magnetostrictive bending of a coated cantilever, *Appl. Phys. Lett.* 70 (19) (1997) 2607–2609. doi:10.1063/1.118932.

Appendix A. Capacitive cantilever method

For the cantilever structure and very thin film with a thickness below 100 nm, the central part of the reaction to the magnetoelastic stress is in the substrate since the elastic contribution of the films can be disregarded compared to that of the substrate. Therefore, the resulting variation of the cantilever radii of curvatures R_x and R_y is related to the magnetoelastic stress of the film. However, λ is presented in some cases [53], but it requires knowledge of the c 's, which is difficult to obtain in some cases.

Considering the ME stress energy for cubic symmetry of the system studied here, which is expressed in a Cartesian coordinate system as:

$$e_{mel} = B_1 \left[\left(\alpha_z^2 - \frac{1}{3} \right) \left(\epsilon_{zz} - \frac{\epsilon_{xx} + \epsilon_{yy}}{2} \right) + \frac{1}{2} \left(\alpha_x^2 - \alpha_y^2 \right) \left(\epsilon_{xx} - \epsilon_{yy} \right) \right] + 2B_2 \left(\alpha_x \alpha_y \epsilon_{xy} + \alpha_y \alpha_z \epsilon_{yz} + \alpha_z \alpha_x \epsilon_{zx} \right) \quad (\text{A.1})$$

with α 's cosines of the magnetization. In the case of the magnetization confined in the xy plane: $\alpha_z = 0$, $\alpha_x = \cos \phi$, $\alpha_y = \sin \phi$, and

$$e_{mel}(\phi) = \frac{1}{2} B_1 \left(\epsilon_{xx} - \epsilon_{yy} \right) \cos 2\phi + B_2 \epsilon_{xy} \sin 2\phi + cte \quad (\text{A.2})$$

The expression for x and y parallel to FeGa[110] and [1-10] directions yields:

$$e_{mel}(\phi) = \frac{1}{2} B_2 \left(\epsilon_{xx} - \epsilon_{yy} \right) \cos 2\phi + B_1 \epsilon_{xy} \sin 2\phi + cte \quad (\text{A.3})$$

Therefore, e_{mel} , with $\epsilon_{xx} \propto R_x^{-1}$, $\epsilon_{yy} \propto R_y^{-1}$ and by energy minimization [54], the relationship between B_1 and B_2 with experiments performed in films with [100] and [110] axes along the cantilever edges are [37, 38]:

$$B_i = \frac{1}{6} E_i \frac{h_{subs}^2}{h_{film}} \Delta \left(\frac{1}{R} \right) \quad (\text{A.4})$$

with $\Delta(1/R)$ is the variation of radii of curvature with the magnetization oriented parallel ($\phi = 0$) and transversely ($\phi = \pi/2$) to the beam directions, with h_{subs} and h_{film} substrate and films thicknesses. The effect of the substrate elastic stiffness coefficients is included in the E_i coefficient, a function of Young's modulus and Poisson ratio at each reference system. Several models [53, 55] and finite elements calculations[56] have been discussed in the literature to determine the role of the transverse curvature of the beam. All of them provide values for E_i as a function of the length/wide ratio but within the range determined by the free, $E_{free} = E/(1+\nu)$, and flat, $E_{flat} = E/(1-\nu^2)$, approximations for the transverse curvature. For the MgO(001), and B_1 , $E_{110} = 318.8$ GPa and $\nu_{110} = 0.03$ with $E \approx E_{flat} \approx E_{free}$. To determine B_2 , $E_{100} = 250$ GPa and $\nu_{100} = 0.24$ with $E_{flat} = 264.5$ GPa and $E_{free} = 201.8$ GPa. For the aspect ratio of the cantilevers used here (≈ 0.6), the value $E_2 = 215$ GPa is obtained from ref. [56].

The clamped MgO substrate covers a fixed electrode entirely. Thus, the capacitance C is given by $C = \epsilon_0 \int [D + \delta(x,y)]^{-1} dx dy$ with the integral extended to the fixed capacitor's electrode area with length L and width w , D is the distance between parallel plates without magnetoelastic contribution, $\delta(x,y)$ is the plate deflection at (x,y) coordinates and ϵ_0 the vacuum permeability constant. Because $\delta(x,y)$ is small the Taylor series approximation can be used.

For a flat cantilever, $\delta(x,y) = 2x^2 R_x^{-1}$ with the capacitance variation $\Delta C = -C_0^2 (6\epsilon_0 f(A) R_x)^{-1}$ and $f(A) = w(L_f - L_i)^2 (L_f^3 - L_i^3)^{-1}$ a function obtained considering the smaller capacitor electrode area. Boundaries for y are $\pm w/2$ (w is the capacitor's smaller plate width) while for x , L_i and $L_f = L_i + L$, the distances between the clamping line and the capacitor fixed electrode edges. All the films used in this study were grown on rectangular substrates 6 mm wide and 20 mm long. Thus, L_f is about 9.8 mm, $L_i \approx 0.8$ mm, and $w = 4$ mm for all samples.

To estimate the role of the transverse curvature in the capacitance values, the transverse deflection of a free plate, $2y^2 R_y^{-1}$, is added to $\delta(x,y)$. Its contribution to the flat cantilever capacitance is (considering $R_x = -R_y$) $0.25w^2(L_f - L_i)(L_f^3 - L_i^3)^{-1}$, a correction as small as ~ 0.038 . It decreases if R_y evolves from infinite at the clamping line to the free end value at a certain large value of L_f . The small effect of the traverse curvature is clear because the sign of the capacitance variation jibes with the ME stress coefficient sign. Therefore, the variation of capacitance at the angular positions zero and $\pi/2$ in Figure 6 is linked to the ME coupling coefficient as:

$$B_i = E_i \frac{h_{subs}^2}{h_{film}} \frac{\epsilon_0 f(A)}{C_0^2} [C(\pi/2) - C(0)] \quad (A.5)$$